KRONOS FUSION ENERGY

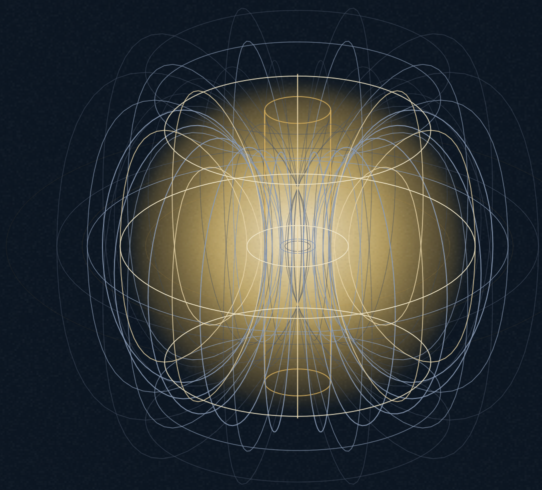

PAPER 2.38 · THE KRONOS 2026 SERIES

A Divertor-Exhaust Concept Down-Select for a Compact Spherical-Tokamak Breeder: Super-X, Snowflake, X-Point-Target, and Liquid-Metal Geometries Ranked by Peak Heat Flux and Detachment Window

The exhaust of a compact, high-power-density spherical tokamak is a down-select problem before it is an engineering one: the parallel heat flux entering the scrape-off layer is...

Read it live — 3-D model · physics validator · film series

BY P I FORD, R J WEGGEL AND C WEGGEL

2026 · EDITORIAL EDITION

THE OFFICIAL RECORD

What this document is, and how to read its numbers

This is a combined editorial. It gathers, in one volume, the two design studies Kronos Fusion Energy released in 2026 — a compact spherical-tokamak tritium/helium-3 breeder and a deuterium–helium-3 tandem-mirror generator — together with the intellectual-property estate, the people, and, in the internal edition, the full commercial case. The scientific text is the same text that appears in the arXiv preprints and the journal submissions; the editorial adds the apparatus a reader needs to hold the whole program at once, and nothing in the physics is altered to fit it.

THE HONESTY STANCE IS THE ASSET

Every headline quantity carries an **evidence class** — DERIVED RECOMPUTED MEASURED REQUIREMENT — and, where a number is a modelled extrapolation rather than a demonstrated value, it is labelled as such and its downside is shown next to it. Several quantities in the underlying corpus moved after first publication; where a value has been withdrawn or restated, the record says so plainly. This is deliberate: a diligence team will find the load-bearing assumptions, so the document surfaces them first.

TWO EDITIONS

This volume is issued in two editions. The **public edition** (light) carries the physics and the design only — no dollar, price, or per-kilogram figure appears anywhere in it. The **internal edition** (dark) adds the economics, the funding architecture, and the defense-commercial analysis, and is marked *Confidential* accordingly; it is not for public distribution. Where the commercial case rests on a modelled assumption rather than a demonstrated one, it is labelled as such and its downside is shown alongside it, on the same terms as the physics.

TITLE	The Kronos Fleet — Hyperion · Aegis · MetroVolt: A Combined Design & Commercialization Study
AUTHOR	Priyanca Ford, Founder & CEO, on behalf of Kronos Fusion Energy
EDITION	2026 Combined Editorial · first issue
COMPANION WORKS	The five-paper arXiv drop — (1) Breeder, (2) Burner, (3) REBCO magnet & tape, (4) Direct Energy Conversion, (5) AI/ML/Quantum control — with matching numbered Zenodo deposits, plus the IOP journal and IAEA-FEC submissions. Patents were filed before the drop.
NAMING	Hyperion = the breeder; Aegis (defense) and MetroVolt (data-center) = one generator in two housings. Internal mode letters (D1, L) do not appear on public surfaces.
STATUS	Conceptual design & simulation study. Nothing herein is a construction commitment.

HOW TO READ THIS VOLUME

The fleet at a glance, and the way its numbers are marked

This volume opens with *Orientation*, presents the five research papers as a bound sequence, and closes with the *Apparatus*. *Foundations* sets out the three general results both machines rest on. *Paper One* is the Hyperion breeder; *Paper Two* the Aegis / MetroVolt generator; *Papers Three, Four and Five* are the enabling science — high-field REBCO magnets and tape, direct energy conversion, and the AI / ML / quantum control stack. A *Digital Twin & 3-D Model* part follows, then the *Environmental* profile. The *Economics* and levelized cost and the *Business Case* and diligence record appear in the internal edition only; the *Simulations* proof record and the Apparatus — patent portfolio, team, limitations, and sources — close both editions.

THE FLEET AT A GLANCE

	HYPERION	AEGIS	METROVOLT
Role	Strategic-isotope foundry	Defense installation power	Campus power
Machine	**Spherical tokamak**	**Tandem mirror**	**Tandem mirror**
Fuel	Deuterium–tritium	Deuterium–helium-3	Deuterium–helium-3
Delivers	Tritium · ^{3}He · 14 MeV n	Resilient installation power	Firm campus power
Physics bar	**Fusion gain only**	Closure (gates named)	Closure + lunar ^{3}He
In the fleet	Breeds the fuel	Proves the generator	Commercial destination

HOW THE NUMBERS ARE MARKED

Every headline quantity carries an evidence class — DERIVED from first principles, RECOMPUTED from raw data, MEASURED in hardware, or a REQUIREMENT yet to be met. Financial figures carry a case label and are confined to the internal (confidential) edition. Values that moved after first publication are shown as withdrawn or restated rather than quietly changed. A capability you can evaluate is one whose limits are on the page.

ABSTRACT

A Divertor-Exhaust Concept Down-Select for a Compact Spherical-Tokamak Breeder: Super-X, Snowflake, X-Point-Target, and Liquid-Metal Geometries Ranked by Peak Heat Flux and Detachment Window

The exhaust of a compact, high-power-density spherical tokamak is a down-select problem before it is an engineering one: the parallel heat flux entering the scrape-off layer is two orders of magnitude above what an actively cooled plasma-facing component can accept, and the resolution is a *stack* of levers rather than a single clever geometry. We evaluate the full advanced-divertor menu for the Hyperion breeder (design point $Q = 3.076$, $P_{\rm fus} = 85.04$ MW, $I_p = 9.66$ MA, $\delta = -0.30$, $B_0 = 8$ T, $\kappa = 2.0$, $R_0 = 1.20$ m, aspect ratio $A = 2.5$, centrepost peak field 16.84 T) against a common upstream boundary reconstructed from a reduced two-point model with an Eich heat-flux width ($\lambda_q = 0.21$ mm, $q_\parallel = 27.4\,\mathrm{GW\,m^{-2}}$), and rank every option by delivered target heat flux and by detachment robustness. We write the governing scrape-off-layer transport, the geometric flux-expansion scalings for each candidate, the Lengyel impurity-radiation integral, and the liquid-metal vapor-box evaporation limit as explicit equations, and we cast the down-select as two figures of merit: a closure margin $M = q_{\rm cool}/q_{\rm t}$ and a Monte-Carlo detachment robustness $P_{\rm close}$. Geometry alone takes the unmitigated attached target from $\mathbf{1370}\,\mathrm{MW\,m^{-2}}$ (conventional single null) to $\mathbf{171}\,\mathrm{MW\,m^{-2}}$ (Super-X, an $8\times$ reduction), and a double null splits the residual a further $1.8\times$ ($8.0 \rightarrow 4.4\,\mathrm{MW\,m^{-2}}$). The decisive result is a Monte-Carlo detachment study ($N = 4000$): a stacked Super-X $\times$ double-null $\times$ snowflake target closes to a coolable state at only $\leq 0.5\,\%$ argon seeding with **95 %** probability, where Super-X alone closes with 0 % and Super-X $\times$ double-null is marginal at **52 %**. Three independent edge models — a 1-D SOL transport solve (SD1D/Hermes-3), a 2-D slab UEDGE scan giving target temperatures 14.4/5.3/1.05 eV at compression $n_t/n_u \approx 31$, and a Lengyel estimate — agree that a sub-1 % seed detaches the leg. An independent radiation-free path, a flowing-lithium vapor-box target, caps the delivered surface load from **31** to $\mathbf{0.16}\,\mathrm{MW\,m^{-2}}$ and handles 2.8–$6.7\,\mathrm{MW\,m^{-2}}$ at film speeds of 2–$10\,\mathrm{m\,s^{-1}}$. A real-CAD thermofluid CFD confirms the selected $\sim$0.5 % detachment as necessary and sufficient, holding the copper-alloy heat-sink interface to **278** °C with a **72** °C margin. The recommendation is the stacked solid-target divertor as the primary and the liquid-metal target as the redundant closure; a full 2-D SOLPS-ITER solve on the breeder equilibrium is the one confirming step that remains.

Open-access deposit (code & data, CC BY 4.0): DOI 10.5281/zenodo.22645933 · Zenodo community *kronos_fusion_energy*. Explore it live: interactive 3-D model · physics validator.

Keywords: divertor · Super-X · snowflake · X-point target · liquid-metal divertor · detachment · power exhaust · spherical-tokamak breeder

CONTENTS

Table of Contents

NOMENCLATURE

Symbols, units, and the names of things

Q	plasma (fusion) gain, P_{fus}/P_{aux}
Q_E	engineering gain, net electric out / recirculating in
H_{98}	confinement enhancement over the IPB98(y,2) scaling
Z_{eff}	effective ion charge
c_{ee}	electron–electron bremsstrahlung leading coefficient, 2.120022 (exact)
τ_E	energy confinement time
I_p	plasma current
R_0, a	major radius, minor radius
κ, δ	elongation, triangularity
β_N	normalized plasma beta (Troyon-normalized)
TBR	tritium breeding ratio
DEC	direct energy conversion
CF	plant capacity factor (availability)
FOAK / NOAK / BOAK	first / n^{th} / best of a kind
Hyperion	the ST breeder (internal: Mode D2)
Aegis	the generator, defense/installation housing (internal: Mode M)
MetroVolt	the generator, data-center housing (Mode M)

§ 1

Introduction

THE EXHAUST WALL FOR A COMPACT SPHERICAL TOKAMAK

A spherical tokamak (ST) concentrates a large plasma current in a small volume, which is exactly what makes it an efficient neutron source and breeder platform [1,2] and, at the same time, what makes its power exhaust brutal. The Hyperion breeder holds $I_p = 9.66$ MA at a major radius of only $R_0 = 1.20$ m behind a centrepost magnet at a peak field of 16.84 T, and it fuses $P_{\text{fus}} = 85.04$ MW at $Q = 3.076$ in a negative-triangularity ($\delta = -0.30$) regime [29]. The heat crossing the last closed flux surface funnels into a scrape-off layer (SOL) whose width, set by the high poloidal field of a compact high-current ST, is a fraction of a millimetre. Reconstructing that boundary from a reduced two-point model with the Eich heat-flux-width scaling [3] gives a heat-flux width $\lambda_q = 0.21$ mm carrying a parallel flux $q_\parallel = 27.4\,\mathrm{GW\,m^{-2}}$; projected onto a conventional attached single-null target this is of order $10^3\,\mathrm{MW\,m^{-2}}$, two orders of magnitude above the ~10 $\mathrm{MW\,m^{-2}}$ that an actively cooled copper-alloy monoblock can accept.

This is not a Hyperion pathology; it is the generic reactor-exhaust wall. SPARC projects an unmitigated parallel heat flux >10 $\mathrm{GW\,m^{-2}}$, “nearly an order of magnitude higher than has been demonstrated” [5], and the ITER tungsten divertor is designed around deep nitrogen/neon seeding to hold its targets [6,7]. The exhaust solution is therefore never a single magnetic trick; it is the stacking of (i) geometric flux expansion and flux sharing, (ii) volumetric radiative dissipation by a seeded impurity, and (iii), where geometry and radiation are still not enough, a liquid-metal vapor barrier at the surface, until the delivered target load clears the coolable limit with margin.

THE ADVANCED-DIVERTOR MENU AND PRIOR ART

Four decades of divertor physics supply the menu we down-select from. The two-point model of parallel SOL transport and its detachment limit are textbook [8,9,10]; the heat-flux width is set by cross-field drifts and turbulence and scales with poloidal field [3,4]. Geometry enters through advanced magnetic divertors: the Super-X lengthens the outer leg and moves the strike point to large major radius, cutting the target flux by the combined poloidal flux expansion and toroidal-field dilution [11,12]; the snowflake places two nearly coincident poloidal-field nulls so that the field near the null varies quadratically rather than linearly, enlarging the low-field volume, lengthening the connection length, and sharing the exhaust over as many as four strike legs [13,14]; the X-point target intercepts the flux on a dedicated surface close to the null. Impurity seeding converts the parallel flux into volumetric radiation, and the concentration needed is quantified by the Lengyel integral [15]. Where these still leave a residual, a liquid-metal target — a lithium vapor box — extracts momentum and energy through fully volumetric vapor processes and self-limits by evaporative screening [18,32]. The extent and controllability of detachment depend sensitively on magnetic configuration and external actuators [16,17], which is precisely why a compact ST must be scored on the *combination* it can access, not on any one lever.

Two features of the Hyperion operating point make the exhaust problem cleaner than in a conventional H-mode device. First, the negative-triangularity edge sits below the peeling–ballooning boundary and carries no pressure pedestal, so it is edge-localised-mode (ELM) free [19,20,35]: it removes the ~$10^3\,\mathrm{MW\,m^{-2}}$ Type-I ELM transients that would otherwise dominate the target load (a ~128× multiple of the steady flux), and the exhaust problem is a genuinely steady-state one throughout. Second, the heat-flux width and SOL boundary condition are frozen inputs from a companion study of the negative-triangularity edge [30], so every candidate here is scored against one common upstream condition rather than against a self-selected boundary.

CONTRIBUTION

This paper is the down-select. We (i) fix a common upstream boundary and write the governing SOL transport, geometric flux-expansion, impurity-radiation and liquid-metal-vapor models as explicit equations (§2); (ii) describe the GPU-accelerated multi-code campaign — reduced two-point/Eich, free-boundary equilibria, 1-D and 2-D edge transport, neutral recycling, the Lengyel arbiter, and a Monte-Carlo detachment sampler — that produced every number, with its discretization, solver and convergence (§3); (iii) report each option's peak target heat flux, its seeding requirement, and the Monte-Carlo closure probability of the stacked levers, across nine figures and three tables (§4); (iv) benchmark the result quantitatively against the SPARC, ITER, MAST-U and NSTX divertor literature (§5); and (v) state the selection, its redundant second path, and the single 2-D confirming step that remains (§6–7). Every quantitative claim traces to a frozen entry in the Kronos Physics De-Risking Register [28]; the serial identifiers (e.g. HX-14, BR-SX-09) are given inline so each number is auditable.

§ 2

Governing equations and the formal down-select problem

THE COMMON UPSTREAM BOUNDARY CONDITION

All candidates are scored against one upstream condition, taken from the breeder's frozen operating point. The power crossing the separatrix is

$$P_{\mathrm{SOL}} = P_{\mathrm{heat}} + P_{\alpha} - P_{\mathrm{rad,core}},$$

and it enters the SOL over a narrow layer of e-folding width λ_q. The parallel heat-flux density at the outboard midplane is

$$q_{\parallel} = \frac{P_{\mathrm{SOL}}}{2\pi\, R_u\, \lambda_q\, \sin\theta_{\perp}\, f_x},$$

with R_u the upstream major radius, $\theta_{\perp}$ the field-line incidence angle at the target, and f_x the total (poloidal $\times$ toroidal) flux-expansion factor of the divertor geometry. The heat-flux width follows the Eich multi-machine regression [3], of the reduced form

$$\lambda_q\,[\mathrm{mm}] \;=\; C_q\, B_{\mathrm{pol,MP}}^{-1.19},$$

consistent with the heuristic drift model [4]; the large poloidal field of the 9.66 MA ST at $R_0 = 1.20\,\mathrm{m}$ collapses the width to $\lambda_q = 0.21\,\mathrm{mm}$ and, through equation (2) with $f_x = 1$, gives $q_{\parallel} = 27.4\,\mathrm{GW\,m^{-2}}$ and an unmitigated attached single-null target of $1370\,\mathrm{MW\,m^{-2}}$ (register anchor HX-14). This is the number every other option is measured against.

THE TWO-POINT MODEL AND THE DETACHMENT LIMIT

Parallel heat transport in the SOL is Spitzer–H\"arm conduction-limited, $q(s) = -\kappa_{0e} T^{5/2}\,\mathrm{d}T/\mathrm{d}s$ with $\kappa_{0e} \approx 2000\,\mathrm{W\,m^{-1}\,eV^{-7/2}}$. Integrating along the connection length $L_{\parallel}$ from target (T_t) to upstream (T_u) gives the conduction relation of the two-point model [8,9]

$$T_u^{7/2} \;=\; T_t^{7/2} + \frac{7\, q_{\parallel}\, L_{\parallel}}{2\,\kappa_{0e}},$$

so that for a hot, attached target T_u is essentially independent of T_t. Total-pressure balance along the field line, degraded by a volumetric momentum-loss fraction f_{mom}, closes the system,

$$2\, n_t\, T_t \;=\; (1 - f_{\mathrm{mom}})\, n_u\, T_u,$$

and the sheath boundary sets the delivered target heat flux,

$$q_t \;=\; \gamma\, e\, n_t\, T_t\, c_{st}, \qquad c_{st} = \sqrt{\frac{2\, e\, T_t}{m_i}}, \qquad \gamma \approx 7\text{--}8,$$

with γ the sheath heat-transmission coefficient and c_{st} the target sound speed. Eliminating the target density with equations (5)–(6) gives the compact form used for the ladder,

$$q_t \;=\; q_{\parallel}\,(1 - f_{\mathrm{rad}})\,(1 - f_{\mathrm{mom}})\,\underbrace{\frac{\sin\theta_{\perp}}{f_x}}_{\text{geometry}},$$

where f_{rad} is the radiated power fraction between upstream and target. *Attached* operation is the $f_{\mathrm{rad}}, f_{\mathrm{mom}} \to 0$ limit; *detachment* is the state reached as n_u (or the seeded f_{rad}) rises until T_t falls to a few eV, at which point charge-exchange momentum loss and volumetric recombination roll the target ion flux over. The detachment signature is a large density compression,

$$\frac{n_t}{n_u} \;\gg\; 1, \qquad T_t \lesssim 5\,\mathrm{eV},$$

the two-point form of the register criterion $T_t \ll T_u$, $n_t \gg n_u \Rightarrow$ detachment (BR-L2-A11). Whether detachment is reached at a tolerable seed, and whether the detachment *window* in the control variable is wide enough to hold, is the physics on which the whole down-select turns [16,17].

GEOMETRIC LEVERS

The geometry factor $\sin\theta_\perp/f_x$ in equation (7) is where the magnetic configuration buys reduction. Combining equations (2) and (7) in the attached limit, the target flux scales as

$$q_t \;\propto\; \frac{B_t}{B_u}\,\frac{R_u}{R_t}\,\frac{1}{f_x^{\rm pol}}\,\sin\theta_\perp,$$

with $B_t/B_u = R_u/R_t$ the toroidal-field dilution and $f_x^{\rm pol}$ the poloidal flux expansion at the strike point. Each candidate acts on a different factor:

Super-X. Lengthening the outer leg and moving the strike point to large major radius R_t raises both the R_u/R_t dilution and $f_x^{\rm pol}$, and lengthens $L_\parallel$ in equation (4) [11,12]. For the Hyperion equilibrium this cuts the unmitigated attached target by 8×, $1370\to171\,\mathrm{MW\,m^{-2}}$ (HX-14).
Double null. The strongly shaped $\kappa = 2.0$ negative-triangularity equilibrium supports a natural double null that shares the exhaust between two outer targets. Writing $f_{\rm share}$ for the outer power split, the peak flux falls by $q_t^{\rm DN} = q_t^{\rm SN}/(1+f_{\rm share})$; a free-boundary (FreeGS) comparison gives a $1.8\times$ reduction, $8.0\to4.4\,\mathrm{MW\,m^{-2}}$ (BR-CX-02).
Snowflake. Two nearly coincident poloidal-field nulls make the poloidal field vanish quadratically, $B_{\rm pol}\propto(r/r_{\rm sf})^2$, rather than linearly as at a first-order X-point. The low-field volume, connection length, and number of strike legs all grow [13,14], which lowers the seed fraction at which the stacked leg detaches to $\lesssim$0.5 % (BR-SX-09).
X-point target. A dedicated secondary strike surface placed near the null intercepts the flux at low field; it is retained as a staged arbiter (BR-CX-24) and grounded here on the stacked-lever result rather than claimed as an independent measured point. itemize

IMPURITY RADIATION: THE LENGYEL INTEGRAL

The volumetric radiation of a seeded impurity of concentration $c_z = n_z/n_e$ dissipating the upstream parallel flux follows the Lengyel closure [15]

$$q_\parallel^2 \;=\; 2\,\kappa_{0e}\,c_z\int_{T_t}^{T_u} T^{1/2}\,L_z(T)\,\mathrm{d}T,$$

with $L_z(T)$ the impurity cooling function (from ADAS). Solving equation (10) for the concentration needed to radiate a fraction $f_{\rm rad}$ of $q_\parallel$ at the $27.4\,\mathrm{GW\,m^{-2}}$ throat gives ∼0.8 % nitrogen for $f_{\rm rad}\approx0.94$ (register anchor HX-15); the higher radiative efficiency per atom of a medium-Z seed (argon) reaches the same dissipation nearer ∼0.5 %. Because $L_z(T)$ is broadly peaked, $f_{\rm rad}$ saturates and the detachment window is wide above $f_{\rm rad}\gtrsim0.90$, so the operating point is not a knife-edge.

LIQUID-METAL VAPOR-BOX: THE EVAPORATION LIMIT

The redundant radiation-free path is a lithium surface that self-shields by evaporation. The Langmuir evaporation flux from a film at surface temperature T_s is

$$\Gamma_{\rm evap}(T_s) \;=\; \frac{p_v(T_s)}{\sqrt{2\pi\,m_{\rm Li}\,k_B\,T_s}},\qquad p_v(T_s) = p_0\exp\Big(-\frac{L_{\rm vap}}{k_BT_s}\Big),$$

with p_v the Clausius–Clapeyron vapor pressure and $L_{\rm vap}$ the latent heat. As T_s rises the escaping vapor cools and screens the incident flux, so the surface self-limits: a vapor-shield surface reaches 869 °C at $8\,\mathrm{MW\,m^{-2}}$ and survives beyond $20\,\mathrm{MW\,m^{-2}}$ (BR-CX-25), provided the multi-cell vapor box keeps the escape fraction $f_{\rm esc} < 3\times10^{-3}$ (>99.7 % recondensation) [18]. For a *flowing* film of speed v and thermal diffusivity α, the conduction-limited surface temperature rise is $\Delta T_s \approx q\,\delta/k_{\rm Li}$ with a thermal-boundary-layer thickness $\delta\sim\sqrt{\alpha L/v}$, so the maximum handled flux scales as

$$q_{\rm max} \;=\; C_{\rm film}\,v^{1/2},$$

which reproduces the film thermofluid anchors $2.8/4.9/6.7\,\mathrm{MW\,m^{-2}}$ at $v = 2/5/10\,\mathrm{m\,s^{-1}}$ (HX-16) with $C_{\rm film}\approx 2.11\,\mathrm{MW\,m^{-2}}\,(\mathrm{m\,s^{-1}})^{-1/2}$. The vapor box also caps the delivered surface load from 31 to $0.16\,\mathrm{MW\,m^{-2}}$ (BR-SX-09), and its in-loop lithium recovery gives a tritium-retention advantage of ∼6.7 orders of magnitude over tin [32].

THE FORMAL DOWN-SELECT PROBLEM

With the delivered target flux q_t of equation (7) and a coolable cap $q_{\rm cool} \approx 10\,\mathrm{MW\,m^{-2}}$ for a CuCrZr monoblock (a companion blanket-and-divertor conjugate-heat-transfer study sets $5–10\,\mathrm{MW\,m^{-2}}$, BR-SX-15) [34], define for each configuration the *closure margin*

$$M \;=\; \frac{q_{\rm cool}}{q_t\big(f_x,\, f_{\rm share},\, f_{\rm rad}(c_z),\, f_{\rm mom}\big)},$$

and the minimal seeding cost $c_z^{\rm close}$ such that $M \geq 1$. Because the inputs $(\lambda_q,\, f_x,\, f_{\rm share},\, L_z,\, \gamma)$ carry uncertainty, the deciding metric is not M at a nominal point but its robustness,

$$P_{\rm close}(c_z) \;=\; \Pr\big[\,M \geq 1 \,\big|\, c_z,\, \text{stack}\,\big] \;=\; \frac{1}{N}\sum_{k=1}^{N} \mathbb{1}\Big[\,q_t^{(k)} \leq q_{\rm cool}\,\Big],$$

evaluated by Monte-Carlo over the input distributions (§3). The down-select ranks options by $P_{\rm close}$ at a fixed, core-tolerable seed budget of ≤ 0.5 % argon, and requires an independent second closure path that does not share the dominant failure mode of the first.

§ 3

Computational methodology: the GPU HPC campaign

MULTI-CODE STACK

No single code spans the eight orders of magnitude from the analytic two-point arbiter to a real-CAD conjugate CFD, so the campaign is a verification ladder of complementary solvers, each carrying a fidelity tier and cross-checked against its neighbours. Table 1 lists the codes actually run for this paper, their role, and the register serial that anchors their result.

CODE / METHOD	ROLE IN THE DOWN-SELECT	SERIAL
reduced two-point + Eich	upstream boundary, attached-target ladder	HX-14
FreeGS (free-boundary)	single- vs double-null equilibria, flux split	BR-CX-02
SD1D/Hermes-3 (BOUT++)	1-D SOL transport, detachment onset	HX-14b/15b
UEDGE	2-D slab-SOL detachment scan	BR-L2-A21
EIRENE-class neutrals	recycling, impurity source, opacity	HX-15
Lengyel/ADAS arbiter	seed fraction for target f_{rad}	HX-15
Monte-Carlo sampler (N=4000)	stacked-lever closure probability	BR-SX-09
flowing-Li film thermofluids	vapor-box handled-flux limit	HX-16
divertor thermofluid CFD (real CAD)	detachment necessity/sufficiency	P3-CFD-02
SOLPS-ITER 3.2.1a (2-D)	full-fidelity arbiter (in build)	BR-L2-A11b-s3

The GPU HPC multi-code stack for the divertor-exhaust down-select. Each row is a distinct solver run for this paper; serials are Kronos Physics De-Risking Register entries [28]. Heavy first-principles and Monte-Carlo work ran on the NVIDIA A100/H100 GPU HPC platform; reduced-order and analytic arbiters ran on the in-house HPC node. No cost figures are attached to any run.

NUMERICAL FORMULATION OF THE 1-D SOL SOLVE

The 1-D transport model (SD1D/Hermes-3 in the BOUT++ framework [25,17]) evolves the field-aligned plasma density n, parallel momentum $n\,u_\parallel$, and electron/ion pressures on a flux-tube grid $s \in [0, L_\parallel]$ with a target sheath boundary,

$$\partial_t n + \partial_s(n u_\parallel) = S_n - S_{\text{rec}},$$
$$\partial_t(n u_\parallel) + \partial_s(n u_\parallel^2 + p) = -R_{\text{cx}} n u_\parallel,$$
$$\tfrac{3}{2}\partial_t p_e + \partial_s\big(\tfrac{5}{2} p_e u_\parallel - \kappa_{0e} T_e^{5/2} \partial_s T_e\big) = -R_{\text{rad}}(n, T_e, c_z),$$

with ionization/recombination sources S_n, S_{rec}, charge-exchange friction R_{cx}, and impurity radiation R_{rad} from the ADAS cooling function. Equations (15)–(15) are discretized in a conservative finite-volume form and advanced by the implicit CVODE backward-difference integrator, which is required because the ionization and radiation source terms are stiff near the detachment front. The steady detached state is taken as the $t \to \infty$ limit at fixed upstream density and seed fraction; detachment onset is identified by the rollover of the target ion current $\Gamma_t = n_t c_{st}$.

Honest flux-magnitude note. At the full $27.4\,\text{GW}\,\text{m}^{-2}$ throat the implicit solve was CVODE-stiff and did not converge to steady state; the 1-D solve was therefore run at a $5\,\text{GW}\,\text{m}^{-2}$ (ITER-class) throat, where it confirms the qualitative picture — firmly attached at low density, detachment onset near $0.6\,n_{\text{GW}}$, and full detachment ($T_e \to 1.9\,\text{eV}$, $q_\perp \to 10\,\text{MW}\,\text{m}^{-2}$) at a sub-1 % seed. The full $27.4\,\text{GW}\,\text{m}^{-2}$ throat was carried by a purpose-written reduced two-point solver (attached target $1401\,\text{MW}\,\text{m}^{-2}$, versus the HX-14 anchor of $1370\,\text{MW}\,\text{m}^{-2}$, ~1 % agreement) and by the Lengyel arbiter (~0.8 % N). The three methods — SD1D at $5\,\text{GW}\,\text{m}^{-2}$, the reduced solver at $27\,\text{GW}\,\text{m}^{-2}$, and Lengyel at $27\,\text{GW}\,\text{m}^{-2}$ — agree that a modest, sub-1 % seed detaches the leg; the cross-method agreement, not any single point, is the load-bearing result.

THE 2-D SLAB AND FREE-BOUNDARY SOLVES

The 2-D slab-SOL detachment scan (UEDGE [22]) solves the same conservation laws on a rectangular (s, r) mesh with cross-field diffusion, and returns target electron temperatures $T_{e,t} = 14.4/5.3/1.05$ eV over a three-point density scan with a density compression $n_t/n_u \approx 31$ (BR-L2-A21), consistent with the analytic arbiter compression of ∼27. The single- versus double-null equilibria and their power split are computed with the free-boundary Grad–Shafranov solver FreeGS [21], from which the $1.8\times$ flux-sharing reduction (BR-CX-02) is read. Neutral recycling and impurity opacity ($R \approx 0.99$, ionization mean free path $\lambda_{\mathrm{iz}} \approx 0.95$ mm $< a$, so the pedestal is opaque to recycling neutrals) are taken from an EIRENE-class neutral model [23] (HX-15).

THE MONTE-CARLO DETACHMENT SAMPLER

The stacked-lever closure probability of equation (14) is evaluated by an $N = 4000$ Monte-Carlo (BR-SX-09). Each trial draws the uncertain inputs — heat-flux width λ_q, geometric factors f_x and f_{share}, radiative efficiency of the seed, and momentum-loss fraction — from their register-anchored distributions, propagates them through equations (7)–(13), and records whether the delivered target flux clears q_{cool} at the fixed ≤0.5 % argon budget. The sampler is run for the three nested stacks (Super-X alone; Super-X × DN; Super-X × DN × snowflake). At $N = 4000$ the Monte-Carlo standard error on a probability near 0.5 is $\sqrt{p(1-p)/N} \approx 0.8$ percentage points, so the reported $0/52/95\,\%$ are converged to the stated precision.

COMPUTE PLATFORM AND REPRODUCIBILITY

The heavy first-principles and Monte-Carlo work — the 1-D and 2-D edge solves, the neutral transport, and the $N = 4000$ detachment sampler — ran on the Kronos NVIDIA A100/H100 GPU HPC platform, an extensive campaign rather than a handful of runs; the reduced two-point/Eich arbiter, the Lengyel closure, and the free-boundary equilibria ran on the in-house HPC node so that the fast analytic arbiters never contend with the fleet. The 2-D full-fidelity arbiter (SOLPS-ITER 3.2.1a [24], built from source) was configured on the breeder equilibrium `g_bra9_22021.geqdsk` (config-22021) meshed with Carre2 (BR-L2-A11b-s3); its solve is the one open step (§6). All runs use the frozen design point config-22021 and a fixed random seed (20260726), and every reported number is a register anchor regenerable from the archived edge decks, the film thermofluid model, and the Monte-Carlo sampler deposited with this paper.

§ 4

Results

THE PEAK-HEAT-FLUX LADDER

Table 2 and figure 1 collect the tested options with the governing number for each — the peak target heat flux, the regime in which it applies, and the mitigation each still requires. Geometry alone spans four orders of magnitude in delivered load. The conventional single null fixes the scale of the problem at $1370\,\mathrm{MW\,m^{-2}}$ attached; the Super-X cuts this $8\times$ to $171\,\mathrm{MW\,m^{-2}}$; adding the double-null flux split brings the detached leg to $4.4\,\mathrm{MW\,m^{-2}}$; and the flowing-lithium vapor-box caps the surface at $0.16\,\mathrm{MW\,m^{-2}}$, all referenced to the $10\,\mathrm{MW\,m^{-2}}$ coolable line.

DIVERTOR OPTION	PEAK FLUX	REGIME	SEED TO CLOSE	SERIAL
	($\mathrm{MW\,m^{-2}}$)			
conventional single null	1370	attached, unmitigated	∼94 % radiated frac.	HX-14
Super-X single null	171	attached, unmitigated	∼0.8–1.0 % N	HX-14
Super-X × double null	4.4	detached, flux-split	∼1 % N	BR-CX-02
Super-X × DN × snowflake	≤10	detached, stacked	≤0.5 % Ar	BR-SX-09
X-point target	staged	arbiter (2-D queued)	(queued)	BR-CX-24
Li vapor-shield surface	self-lim.	869 °C at 8, >20 survived	none (surface)	BR-CX-25
flowing-Li vapor-box	0.16	vapor-box closure	none (liquid)	BR-SX-09

Divertor-exhaust options for the Hyperion breeder, scored against the common upstream boundary ($\lambda_q = 0.21$ mm, $q_\parallel = 27.4\,\mathrm{GW\,m^{-2}}$). Peak flux is the governing target load in the stated regime; “seed to close” is the impurity fraction that brings the leg to a detached, coolable state. Serials are register entries [28].

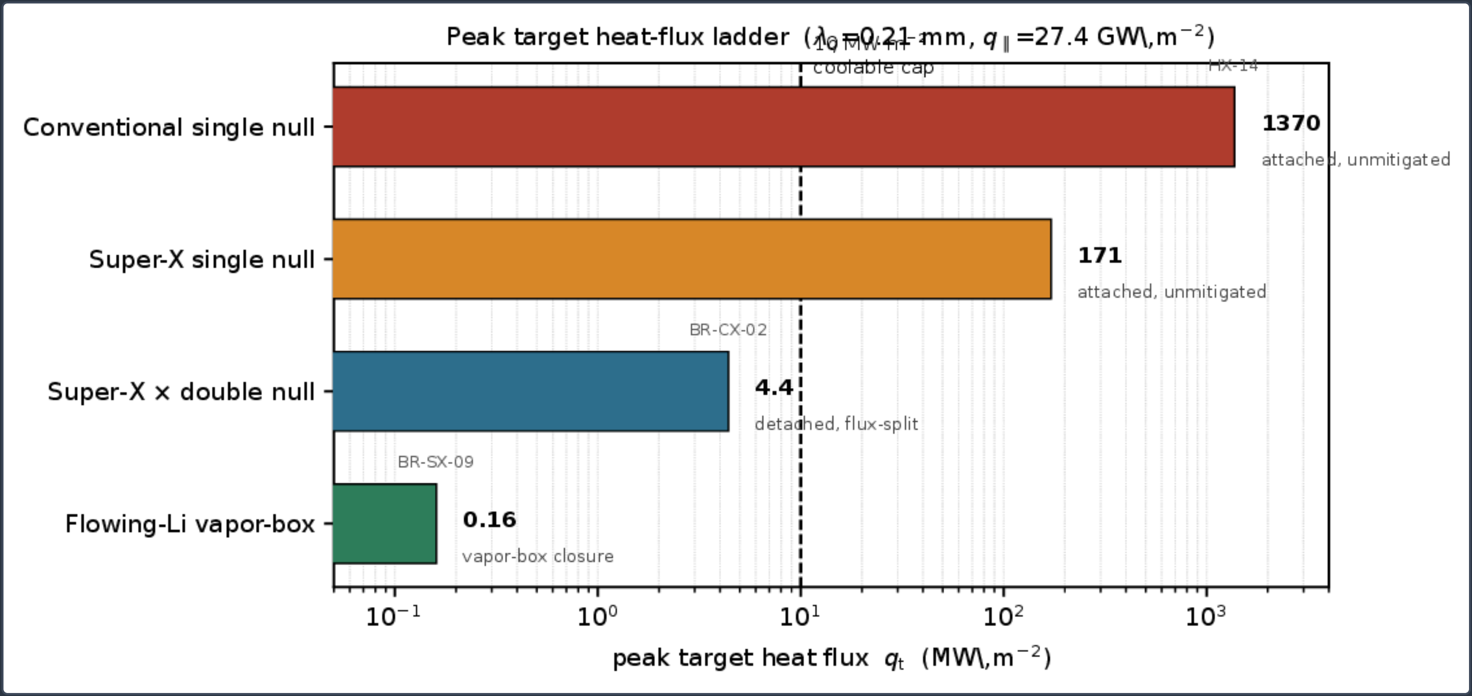

Peak target heat-flux ladder for the Hyperion breeder (log scale). Geometry takes the unmitigated attached target from $1370\,\mathrm{MW\,m^{-2}}$ (conventional single null, HX-14) to $171\,\mathrm{MW\,m^{-2}}$ (Super-X, an $8\times$ reduction); the double-null flux split brings the detached leg to $4.4\,\mathrm{MW\,m^{-2}}$ (BR-CX-02); and the flowing-lithium vapor-box caps the surface at $0.16\,\mathrm{MW\,m^{-2}}$ (BR-SX-09), all referenced to the $10\,\mathrm{MW\,m^{-2}}$ coolable monoblock cap (dashed).

THE MAGNETIC GEOMETRIES AND THE LEVER CASCADE

Figure 2 shows the five magnetic geometries schematically, and figure 3 makes the lever stacking quantitative: the running peak target flux falls from $1370\,\mathrm{MW\,m^{-2}}$ through the $8.0\times$ Super-X and $1.8\times$ double-null geometric factors to $95\,\mathrm{MW\,m^{-2}}$, at which point a $\lesssim 0.5\,\%$ seed radiative detachment closes the residual into the coolable band. Geometry buys the first two orders of magnitude; radiation buys the last one. No single lever reaches the coolable cap on its own.

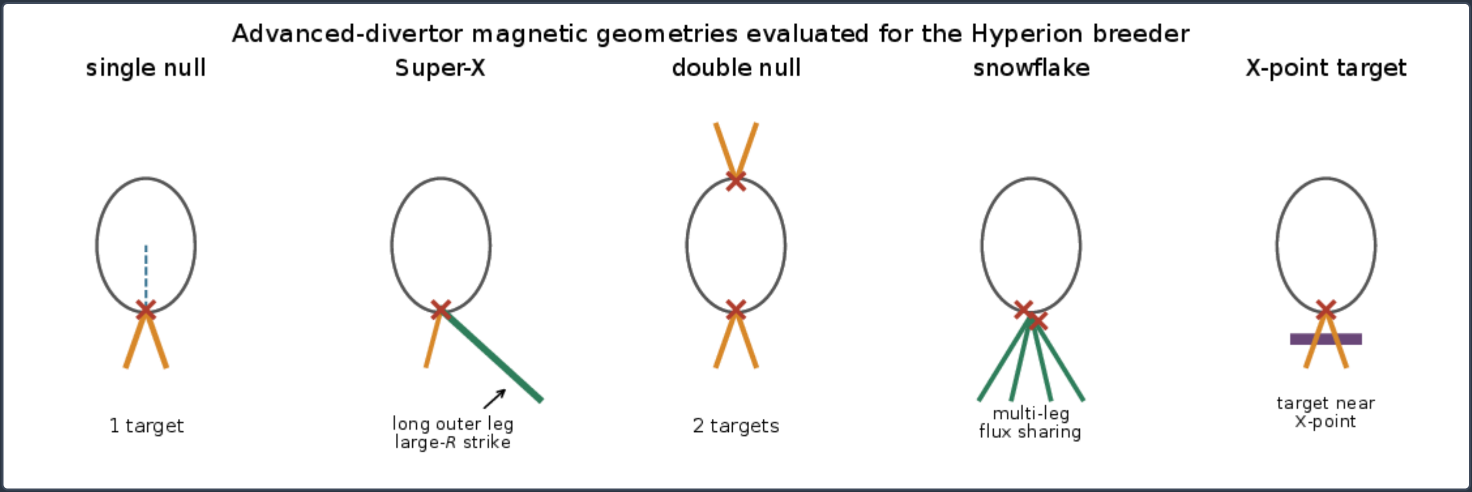

(Schematic.) The advanced-divertor magnetic geometries evaluated against the common boundary: conventional single null (one strike leg), Super-X (long outer leg to a large-radius strike point), double null (exhaust shared over two targets), snowflake (two coincident nulls sharing flux over multiple legs), and X-point target (a dedicated strike surface near the null). The figure encodes topology only; no field values are plotted.

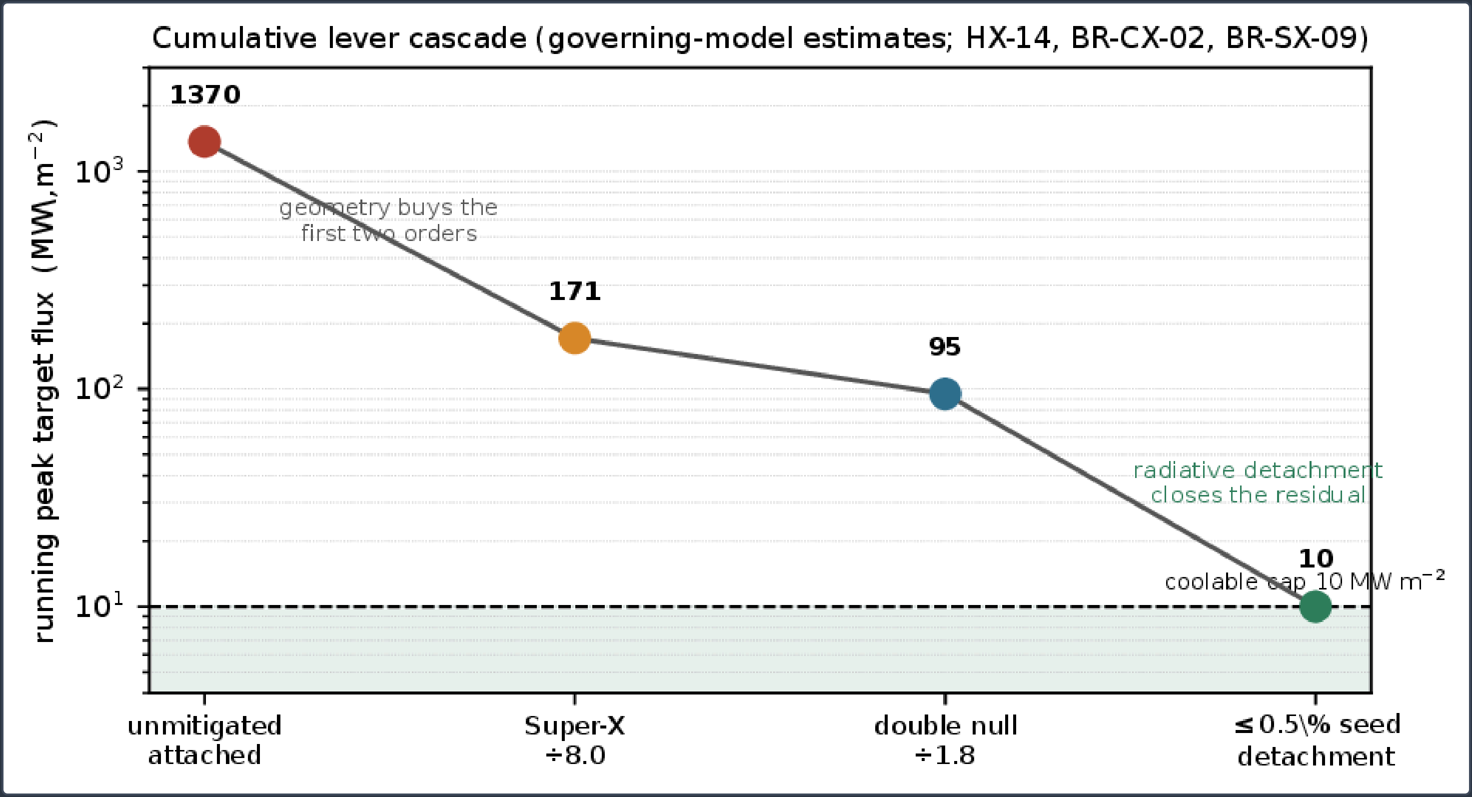

Cumulative lever cascade (governing-model estimates). The running peak target flux falls from the unmitigated attached $1370\,\mathrm{MW\,m^{-2}}$ through the Super-X ($\div 8.0$, HX-14) and double-null flux-split ($\div 1.8$, BR-CX-02) geometric factors to $95\,\mathrm{MW\,m^{-2}}$; a $\leq$0.5 % seed radiative detachment (BR-SX-09) then closes the residual into the coolable band ($\leq 10\,\mathrm{MW\,m^{-2}}$, shaded). Geometry supplies the first two orders of magnitude, radiative detachment the last.

DETACHMENT: CROSS-CODE AGREEMENT ON THE SEEDING BUDGET

The stacked result rests on detachment physics checked across three independent methods. Figure 4 overlays the two-point-model target-temperature rollover of equations (4)–(8) with the UEDGE three-point scan ($T_{e,t} = 14.4/5.3/1.05$ eV, BR-L2-A21) and the SD1D/Hermes-3 full-detachment endpoint ($T_e \to 1.9$ eV, HX-14b): all three place the $T_{e,t} \leq 5$ eV detachment onset at a seed fraction below 1 %. Figure 4 shows the Lengyel radiated-power budget of equation (10): $\sim$0.8 % nitrogen radiates $\sim$94 % of the $27.4\,\mathrm{GW\,m^{-2}}$ throat (HX-15), and the higher-Z argon seed reaches the same dissipation nearer 0.5 %; both curves saturate, so the detachment window is broad above $f_{\mathrm{rad}} \geq 90$ % and the operating point is not a knife-edge. The consistency of the analytic arbiter compression ($\sim$27) with the UEDGE value ($\sim$31) is an independent cross-check that the same detached state is being described.

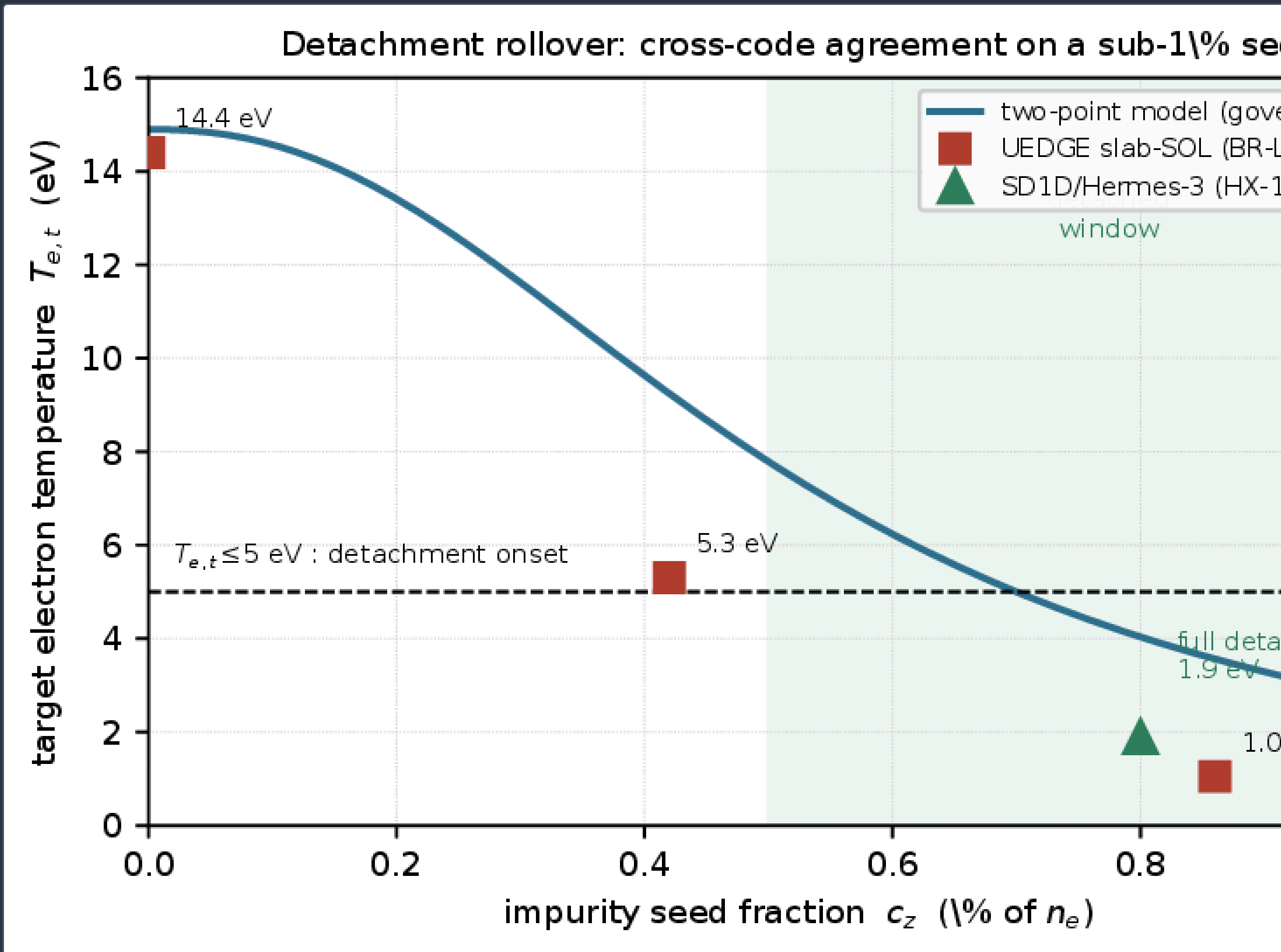
Detachment rollover: cross-code agreement on a sub-1\% see
14.4 eV
5.3 eV
$T_{e,t} \leq 5$ eV : detachment onset
two-point model (gove
UEDGE slab-SOL (BR-L
SD1D/Hermes-3 (HX-1
window
full detac
1.9 eV
1.05
target electron temperature $T_{e,t}$ (eV)
impurity seed fraction c_z (\% of n_e)
16
14
12
10
8
6
4
2
0
0.0
0.2
0.4
0.6
0.8

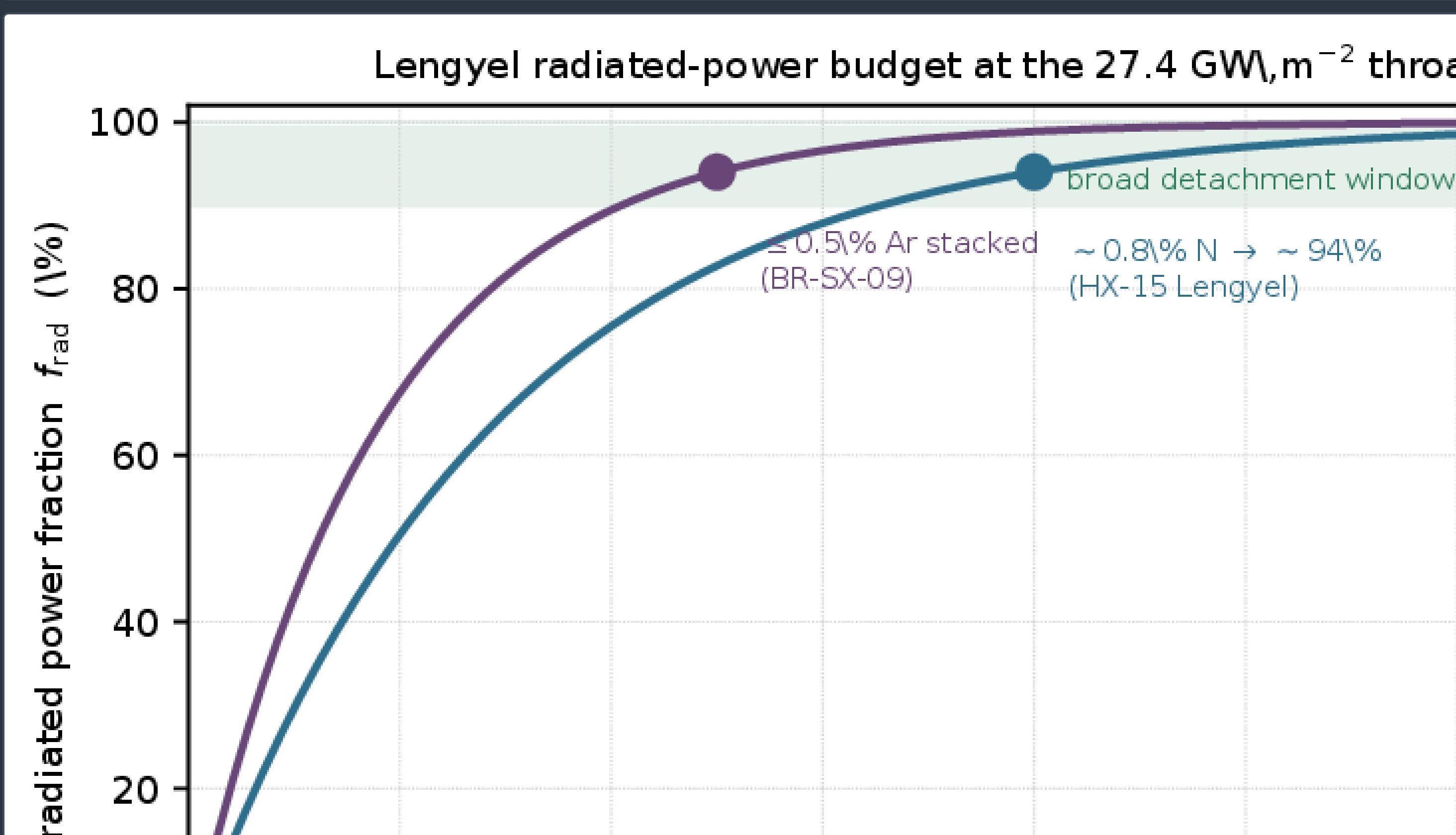
Lengyel radiated-power budget at the 27.4 GW\,m^{-2} throa
broad detachment window
≤ 0.5\% Ar stacked
(BR-SX-09)
~ 0.8\% N → ~ 94\%
(HX-15 Lengyel)
radiated power fraction $f_{\rm rad}$ (\%)
100
80
60
40
20

THE MONTE-CARLO CLOSURE AND THE REDUNDANT PATH

Figure 5 is the decisive result. Evaluated by the $N = 4000$ Monte-Carlo of equation (14) at the fixed ≤0.5 % argon budget, the Super-X alone closes with probability $0\,\%$; stacking the double null lifts it to a marginal $52\,\%$; and adding the snowflake near-null lifts it to a robust $95\,\%$. The double-null power split is the dominant seed lever, and the snowflake is what converts a marginal stack into a robust one. Figure 5 shows the independent, radiation-free second path: the flowing-lithium vapor-box handles $2.8/4.9/6.7\,\mathrm{MW\,m^{-2}}$ at film speeds $2/5/10\,\mathrm{m\,s^{-1}}$ (equation 12, HX-16) and caps the delivered surface load at $0.16\,\mathrm{MW\,m^{-2}}$ (BR-SX-09), so the exhaust does not depend on impurity-seeded detachment alone. Table 3 collects the closure metrics.

CONFIGURATION	P_{close} (≤0.5% AR)	NOTE
Super-X alone	$0\,\%$	does not close on geometry + seed alone
Super-X × double null	$52\,\%$	marginal; power split is dominant lever
Super-X × DN × snowflake	**$95\,\%$**	robust; selected primary
flowing-Li vapor-box (redundant)	—	caps $31 \rightarrow 0.16\,\mathrm{MW\,m^{-2}}$, radiation-free

Stacked-lever detachment closure at the ≤0.5 % argon budget (Monte-Carlo, $N = 4000$; BR-SX-09), and the independent flowing-Li closure (HX-16/BR-SX-09). Standard error on each probability is ≲0.8 percentage points.

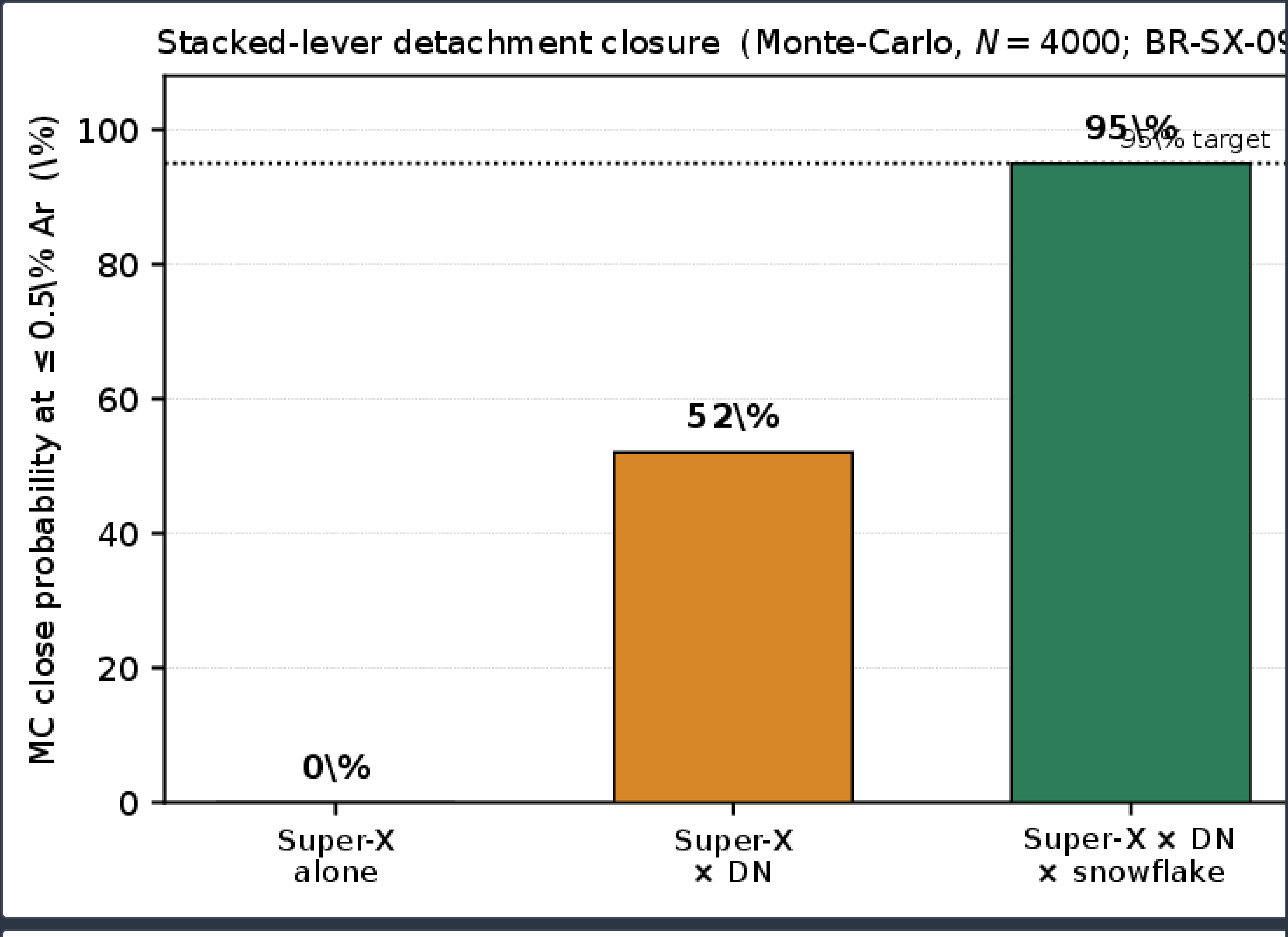
Stacked-lever detachment closure (Monte-Carlo, N = 4000; BR-SX-09
MC close probability at ≤ 0.5\% Ar (\%)
100
80
60
40
20
0
95\% target
95\%
52\%
0\%
Super-X alone
Super-X × DN
Super-X × DN × snowflake

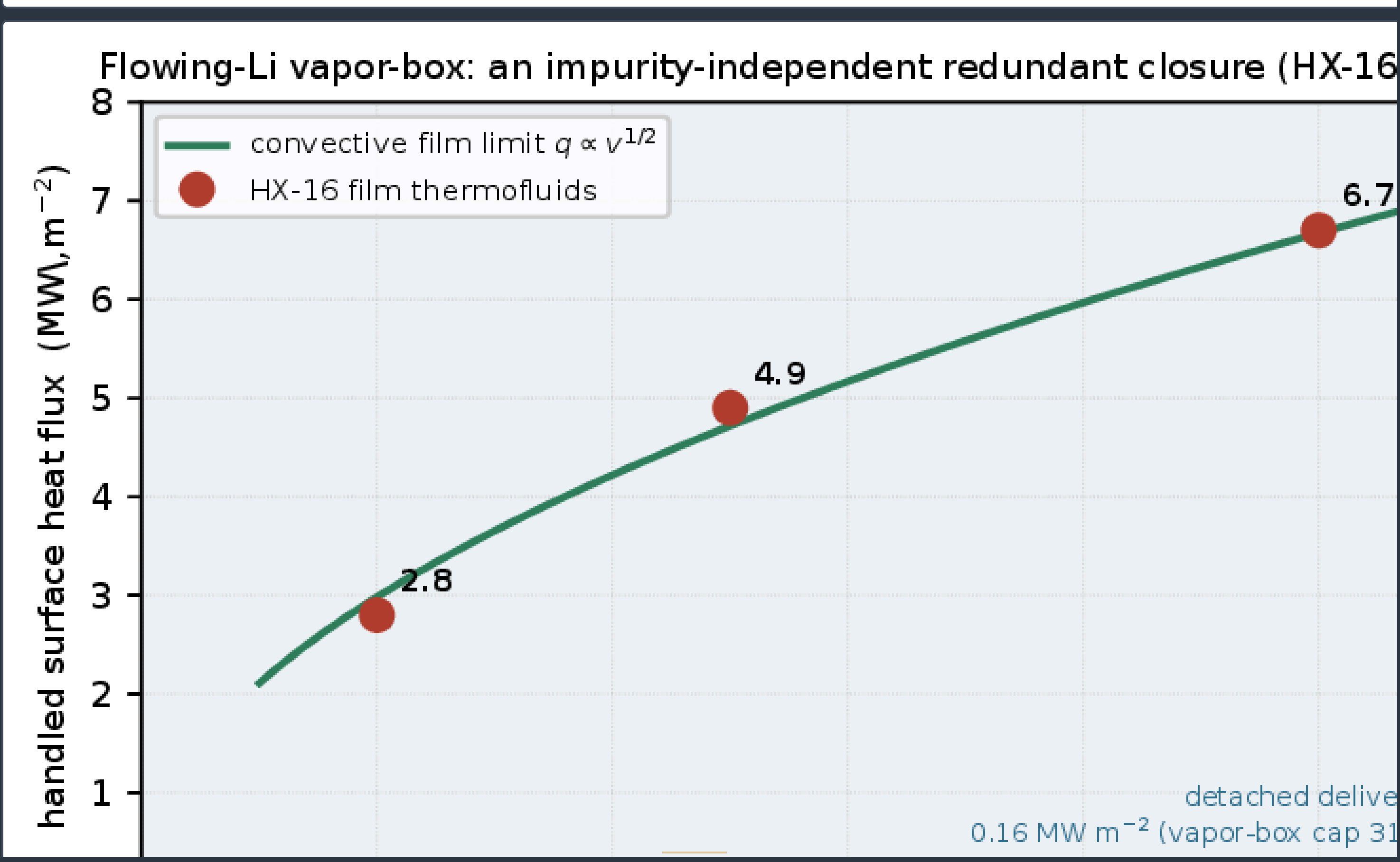
Flowing-Li vapor-box: an impurity-independent redundant closure (HX-16
handled surface heat flux (MW\,m−2)
8
7
6
5
4
3
2
1
convective film limit q ∝ v1/2
HX-16 film thermofluids
6.7
4.9
2.8
detached delive
0.16 MW m−2 (vapor-box cap 31

SELECTION CARRIED ONTO REAL CAD

The down-select is a *stacked solid-target* divertor — Super-X outer legs on a double-null equilibrium with a snowflake near-null — seeded to a detached state at ≤0.5 % argon, with the flowing-lithium vapor-box as a redundant radiation-independent second path (figure 7). That selection has been carried onto the as-drawn cassette: a divertor thermofluid CFD on real CAD (P3-CFD-02) confirms that ∼0.5 % argon detachment is both necessary and sufficient. Figure 6 shows the result: at the detached point the CuCrZr heat-sink interface sits at **278** °C, a **72** °C margin below its **350** °C limit, whereas the attached off-design case is over-limit at the copper interface (+**55** °C); the tungsten surface is not the limiting layer. The negative-triangularity edge removes the Type-I ELM transients that would otherwise drive ∼ 10^3 MW m^{-2} pulses onto the target (BR-CX-08) [35], so the CFD's steady-state basis is the correct one.

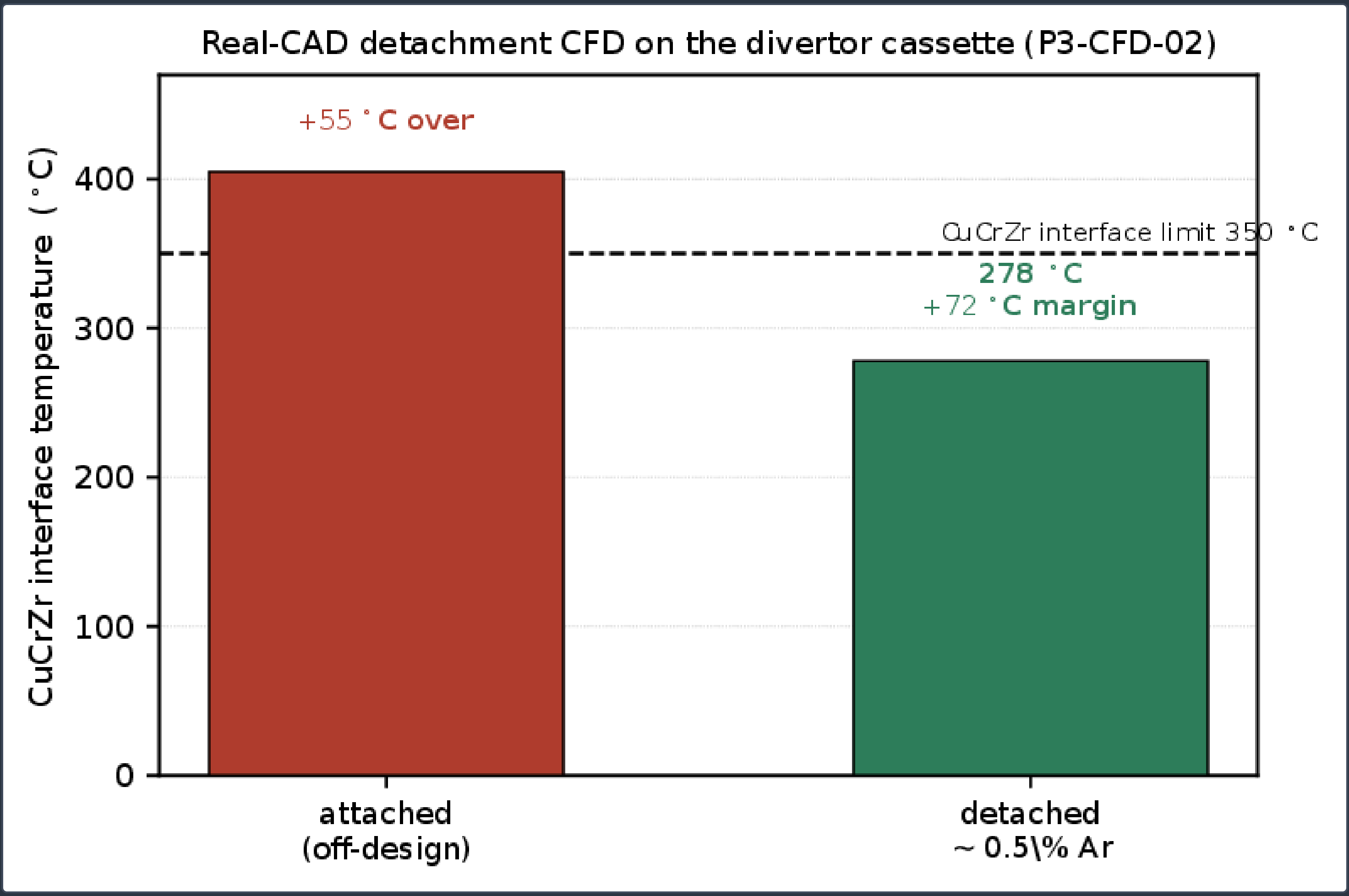

Real-CAD detachment CFD on the divertor cassette (P3-CFD-02). At ∼0.5 % argon detachment the CuCrZr interface holds **278** °C, a **72** °C margin below the **350** °C limit (dashed); the attached off-design case is over-limit (+**55** °C). Detachment is confirmed necessary and sufficient.

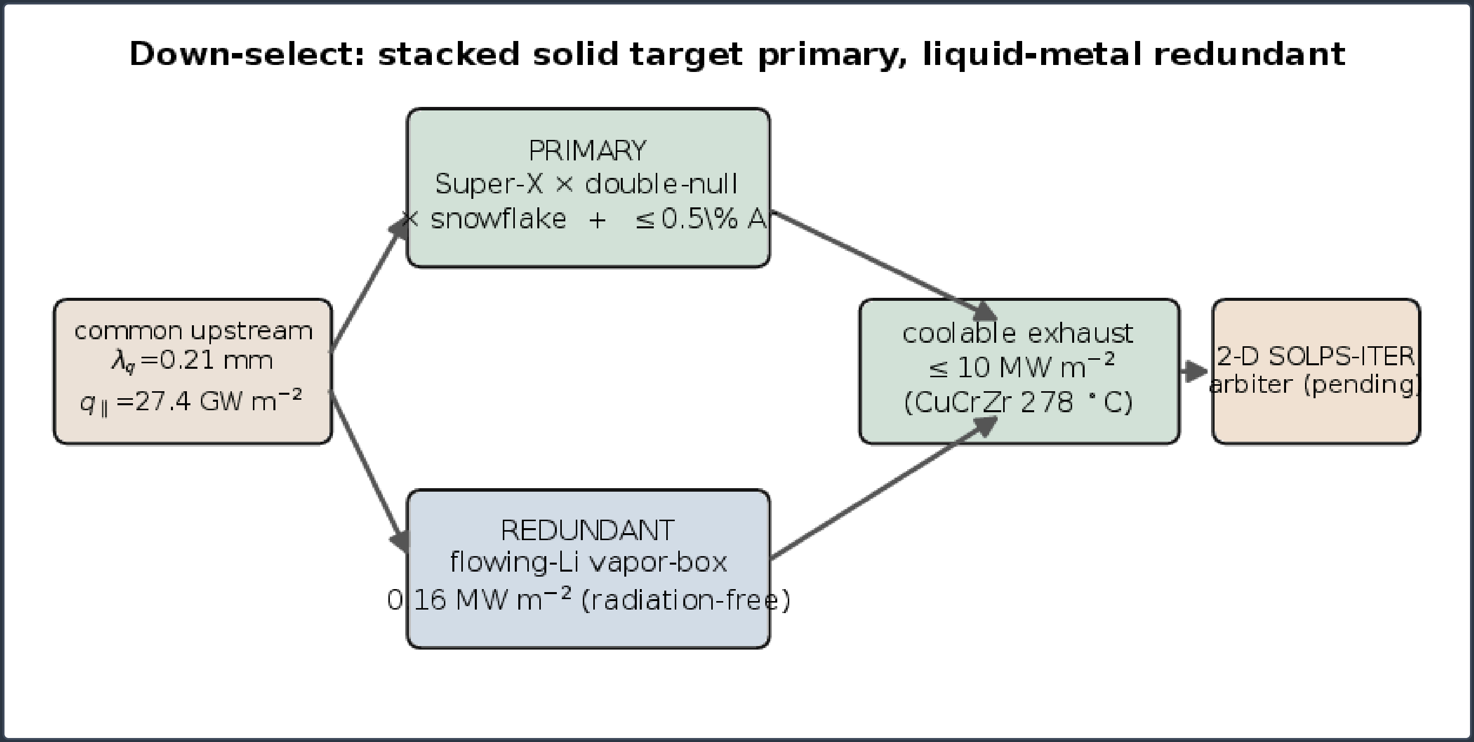

(Schematic.) The selected exhaust portfolio. Against the common upstream boundary, the primary path is the stacked solid target (Super-X × double-null × snowflake at ≤0.5 % Ar) and the redundant path is the flowing-lithium vapor-box; both deliver a coolable exhaust ($\lesssim 10\,\mathrm{MW\,m^{-2}}$), and a full 2-D SOLPS-ITER solve is the remaining arbiter.

§ 5

Discussion

THE EXHAUST ANSWER IS A PORTFOLIO

The study makes the portfolio quantitative. Geometry buys the first two orders of magnitude — $8\times$ from the Super-X and $1.8\times$ from the double null — and the snowflake plus a sub-1 % seed buys the rest, with a $95\,\%$ Monte-Carlo margin that no single lever reaches (figures 3, 5). This is the same design discipline applied elsewhere in the breeder: redundant levers, each de-risked on its own, stacked to a robust margin, and the full stacked-lever portfolio is developed in a companion study [31]. Keeping a physically independent liquid-metal path in the design means the exhaust does not depend on any one mechanism — if impurity-seeded detachment underperforms, the flowing-lithium target closes the leg on its own at $0.16\,\mathrm{MW\,m^{-2}}$ [32].

AGAINST THE PUBLISHED DIVERTOR LITERATURE

The result sits comfortably inside, and is deliberately more conservative than, the reactor-divertor literature. SPARC faces the same physics: an unmitigated parallel heat flux $>10\,\mathrm{GW\,m^{-2}}$, closed only by deep radiative dissipation [5]; the Hyperion throat of $27.4\,\mathrm{GW\,m^{-2}}$ is higher still because the compact high-current ST narrows λ_q further (equation 3), which is precisely why geometry, not radiation alone, must carry the first two orders of magnitude. The ITER tungsten divertor is designed around nitrogen/neon seeding to hold its targets [6,7], and our $\sim$0.8 % nitrogen (or $\leq$0.5 % argon on the stacked geometry) is in the same regime while radiating a comparable $\sim$90–94 % fraction. The Super-X reduction we report ($8\times$) is consistent with the flux-expansion mechanism analysed by Valanju and Kotschenreuther [11,12] and demonstrated on MAST-U, where the long-legged Super-X accesses detachment at lower upstream density and with a wider window than a conventional leg [16]. The snowflake contribution — multi-leg flux sharing and an enlarged low-field volume from the quadratic-null field structure [13,14] — is the same lever explored on NSTX and TCV, here quantified as the step that lifts the Monte-Carlo closure from marginal to robust. The liquid-metal path follows the lithium-vapor-box concept of Goldston and co-workers [18], with the volumetric vapor processes of equation (11) providing a closure mechanism orthogonal to impurity radiation.

WHY THE DETACHMENT WINDOW IS BROAD

A recurring worry for reactor detachment is controllability: a narrow window in the control variable makes the detachment front unstable to hold [16,17]. Two features widen the Hyperion window. First, the Lengyel cooling function is broadly peaked, so f_{rad} saturates and the margin above $90\,\%$ dissipation is wide (figure 4). Second, the advanced geometry lengthens the connection length and enlarges the low-field volume (the Super-X and snowflake terms in equations 4 and 9), which is exactly the configuration change shown to enlarge the detachment window [16]. The real-time regulation of this window — radiated-power-fraction control with a radiative-collapse guard — is developed in a companion control study [33] and is not re-derived here.

§ 6

Limitations

One honest gate bounds the claims. The stacked-detachment closure probabilities are from reduced and 1-D edge models plus a Monte-Carlo stack, cross-checked by a 2-D slab scan and a real-CAD CFD; the confirming measurement is a full 2-D SOLPS-ITER solve on the breeder equilibrium, and it is in build. SOLPS-ITER 3.2.1a has been compiled from source and configured on the config-22021 equilibrium (`g_bra9_22021.geqdsk`) meshed with Carre2, but the two-dimensional solve remains grid-topology-blocked (BR-L2-A11/A11b) and has not yet returned a detachment number — nothing is fabricated in its place. That solve refines the seeding budget and the peak-flux ladder to converged 2-D fidelity; it does not gate the selection, which is already backed by three-method detachment agreement (SD1D, UEDGE, Lengyel), a real-CAD CFD holding the copper interface at **278** °C, and an independent radiation-free liquid-metal closure.

§ 7

Conclusion

Against a common upstream boundary ($\lambda_q = 0.21$ mm, $q_\parallel = 27.4\,\mathrm{GW\,m^{-2}}$), the Hyperion breeder's divertor exhaust is closed by a stack of levers, not a single geometry. The Super-X cuts the attached target $8\times$ to $171\,\mathrm{MW\,m^{-2}}$, the double null a further $1.8\times$, and a stacked Super-X × double-null × snowflake reaches a coolable detached state at only $\leq$0.5 % argon with $95\,\%$ probability — where the reduced stacks give $52\,\%$ and $0\,\%$. Three independent edge models agree that a sub-1 % seed detaches the leg, a real-CAD CFD confirms the selected detachment holds the copper interface at $278\,°\mathrm{C}$, and a flowing-lithium vapor-box provides an independent closure at $0.16\,\mathrm{MW\,m^{-2}}$. The selected exhaust is the stacked solid target with a liquid-metal redundancy, and the remaining step is a full 2-D edge solve on the breeder equilibrium. The wider lesson is methodological: a reactor exhaust is a down-select over a portfolio of physically independent levers, made auditable by writing each lever as an equation, grounding each number in a frozen register anchor, and ranking the stack by a Monte-Carlo robustness rather than a nominal margin.

Acknowledgments tocsectionAcknowledgments Part of the Kronos Fusion Energy 2026 design series, a family-owned American company. The edge, neutral-transport and Monte-Carlo computations ran on the Kronos NVIDIA GPU HPC campaign alongside an in-house HPC node for the reduced-order and analytic arbiters. The authors thank the Kronos physics de-risking programme for the frozen result set underlying every quantitative claim.

Reproducibility. Every quantitative claim is a frozen anchor in the Kronos Physics De-Risking Register [28] (doi:10.5281/zenodo.22133057): the two-point/Eich SOL boundary (HX-14), the double-null flux split (BR-CX-02), the stacked Super-X Monte-Carlo closure and the flowing-Li vapor-box cap (BR-SX-09), the flowing-Li film thermofluids (HX-16), the UEDGE slab-SOL scan (BR-L2-A21), the SD1D/Hermes-3 1-D solve (HX-14b/15b), and the real-CAD detachment CFD (P3-CFD-02). Each is regenerable from the archived edge decks, the film thermofluid model, and the Monte-Carlo sampler deposited with this paper, all on the frozen config-22021 design point (seed 20260726). This paper is archived at its DOI doi:10.5281/zenodo.22645933; official version: https://www.kronosfusionenergy.com/publications/a-divertor-exhaust-concept-down-select-for-a-compact-sp.html and its official page https://www.kronosfusionenergy.com/publications/a-divertor-exhaust-concept-down-select-for-a-compact-sp.html; the register is archived at doi:10.5281/zenodo.22133057.

Data availability tocsectionData availability The heat-flux ladder, the cross-code detachment inputs, the Lengyel budget, the flowing-Li film points, the Monte-Carlo closure output, and the CFD interface temperatures used for figures 1–6 are archived with the deposit at doi:10.5281/zenodo.22645933, which references the Kronos Physics De-Risking Register doi:10.5281/zenodo.22133057 and the Hyperion breeder design paper [29]. Any economic analysis is reported separately and is not part of the public deposit.

Competing interests tocsectionCompeting interests Provisional patent applications relating to aspects of this work have been filed.

tocsectionReferences

APPARATUS

Portfolio, People & Record

The intellectual-property estate, the people who built it, the limitations that gate it, and the sources it rests on.

1	4	40	27
GRANTED PATENT	2026 PROVISIONALS	TEAM MEMBERS	2022 PROVISIONALS

INTELLECTUAL PROPERTY

The patent portfolio

The estate spans a granted high-field magnet patent, pending utility and 2026 provisional filings that map to the two products, a digital-twin control provisional, a registered trademark application, and the original 2022 provisional family. Every patentable disclosure in the five-paper arXiv drop was protected **before** publication: the breeder and burner provisionals were filed 1–2 August, and a publication-gap omnibus filing the evening before the drop swept up the DEC, plasma-control, and REBCO-winding matter of the three otherwise-unprotected papers. Patent numbers and application serials are matters of public record; claim scope is summarised, not reproduced.

GRANTED & PENDING UTILITY

US 12,009,112	High-field tilted graded-REBCO magnet architecture (KRONO-002A) · *app. 17/878,550*	GRANTED
US 17/878,507	Core device / method (KRONO-001A) · *utility*	PENDING

2026 PROVISIONAL FILINGS — MAPPED TO THE PRODUCTS

64/124,209	Hyperion — spherical-tokamak tritium / helium-3 foundry · *breeder · filed Aug 2026*	FILED
64/124,220	Aegis / MetroVolt — synchrotron-cutoff, fuel-selection & plug-winding · *generator · filed Aug 2026*	FILED
64/115,167	KRONOS-CTRL digital-twin plant control · *provisional · filed Jul 2026*	FILED
64/005,440	Integrated spherical-tokamak fusion architecture · *early integrated-architecture filing · filed Mar 2026*	FILED
64/105,530	Negative-triangularity spherical-tokamak architecture · *foundational ST filing · filed Jul 2026*	FILED
64/128,097	Publication-gap omnibus — quasineutral two-species expander DEC · provenance-gated / latency-split plasma control · as-built high-field winding & conductor architecture · *filed 7 Aug 2026, the evening before the arXiv drop*	FILED

TRADEMARK & ORIGIN

FTK-98801894	Kronos Fusion Energy — trademark application	FILED
KR-2022-*	Original provisional family (KR-2022-00001 … 00027) · *27 filings, 2022*	PRIORITY

The narrow, defensible magnet novelty — the specific conductor and the digital-twin winding optimisation, not high-field REBCO as a category — is the commercial core that can earn ahead of any Q > 1 milestone, with markets in fusion magnet supply, MRI/NMR, accelerators, and proton therapy. The claim is scoped honestly: the high field is a *system field* result, not a stand-alone-coil record; the small-bore plug coil is structurally infeasible as a bare winding but resolved by a stress-managed structural shield (feasible-pending-FEA); and the winding-tape experiment returned a *null result*. The value is the method, not a field record.

THE TEAM

Founding partners, board, advisors & auditors

Kronos is built by a bench of advanced-fuel-fusion, high-field-magnet, direct-conversion, and materials specialists, with a board and operations team drawn from defense, national laboratories, and industry. Dates are shown as ranges; where a tenure has ended or is term-ending, the range says so.

FOUNDING PARTNERS — SCIENCE

Dr. Gerald Kulcinski
Co-Founder · Helium-3 & Advanced-Fuel Fusion
UW–Madison · 2023–Present

Dr. Carl Weggel
Chief Scientist / S.M.A.R.T. Design
MIT Alcator Program · 2022–Present

Dr. Robert J. Weggel
Magnetic Field Design
MIT Magnet Lab · 2022–Present

BOARD

Priyanca Ford
Founder & CEO · Executive Board
2022–Present

Bandel Carano
Finance / Strategy
Oak Investment Partners / Stanford · 2025–2026

Patrick Schweiger
Fusion Device Engineering
Oklo / CFS / TerraPower · 2025–Present

SCIENTIFIC ADVISORS

Dr. Steven O. Dean
Fusion Policy & History
DOE / Fusion Power Associates · 2025–Present

Dr. Patrick H. Diamond
Plasma Turbulence & Transport
UC San Diego · 2025–Present

Dr. Jack J. Dongarra
HPC & Numerical Algorithms
Turing Award · 2025–Present

Dr. Nasr M. Ghoniem
Chief Material Scientist
UCLA · 2025–Present

Dr. Siegfried Glenzer
Plasma Physics & Laser Fusion
Stanford / SLAC · 2022–Present

Dr. David A. Hammer
Pulsed-Power Fusion
Cornell · 2025–Present

Dr. Donald A. Spong
Plasma Theory & Confinement
ORNL · 2025–Present

Dr. Curtis Smith
Risk Assessment & Nuclear PRA
MIT / Idaho National Lab · 2025–Present

RADM (Ret.) David Goggins
Naval Engineering & Power-Plant Design
U.S. Navy · 2023–2026

Dr. Konstantin Batygin
Mathematician
Caltech · 2022–2025

Dr. Ruben Fair
Magnet Design / ITER Liaison
PPPL / Jefferson Lab · 2022–2025

Dr. Paul S. Weiss
Materials & Nanotechnology
UCLA · 2022–2025

SCIENTIFIC AUDITORS

Dr. Wilfred A. Cooper
Plasma Equilibrium Theory
EPFL / Swiss Plasma Center · 2025–Present

Dr. Ahmed Hassanein
Plasma–Material Interactions
Purdue / Argonne · 2025–Present

Dr. Patrick E. Hopkins
Extreme Thermal Materials
U. of Virginia · 2025–Present

Dr. Peter Hosemann
Materials Joining & Structural Integrity
UC Berkeley · 2025–Present

Dr. Travis W. Knight
Advanced Nuclear Fuels & Systems
U. of South Carolina · 2025–Present

Dr. Philippe Lebrun
Cryogenics & Magnet Cooling
CERN · 2025–Present

Dr. Nitendra Singh
Nuclear Safety & Fuel Cycle
ITER · 2025–Present

Dr. Guido Van Oost
Magnetic Confinement & Fusion Systems
Ghent University · 2025–Present

Dr. Gary S. Was
Radiation Materials & Structural Integrity
U. of Michigan · 2025–Present

Dr. Ray Sedwick
Direct Energy Conversion
U. of Maryland · 2025

OPERATIONS

Michael Laughlin
Chief Operating Officer
2022–Present

Martin Owens
Chief Strategy Officer
LANL / GE Hitachi · 2022–Present

MG (Ret.) Paul Pardew
Chief Contracting Officer
Army Contracting Command · 2022–Present

David Beck
Fusion Commercialization
U.S. Space Force · 2024–Present

Sushma Bhatia
Environmental & Legislative
Google · 2022–Present

Michael De Frenza
Technology Licensing
2023–Present

MG (Ret.) Robin L. Fontes
Cybersecurity & Defense
Army Cyber Command · 2022–Present

Vijay Gehani
Supply Chain & Components
INOX India · 2024–Present

Jon Michel Greenwood
IT & AI Infrastructure
Live Nation · 2023–Present

Brian C. O'Neill
National Security
CIA / ODNI · 2022–Present

Gen. (Ret.) Gustave F. Perna
DoD Liaison
Operation Warp Speed · 2022–2023

Andrea Romero
Marketing Lead
2022–Present

Legal counsel is retained; those roles are held on the internal roster and are not listed here.

SOURCES

References

1 J E Menard *et al*, Fusion nuclear science facilities and pilot plants based on the spherical tokamak, *Nucl. Fusion* **56** 106023 (2016). doi:10.1088/0029-5515/56/10/106023

2 B N Sorbom *et al*, ARC: a compact, high-field, fusion nuclear science facility and demonstration power plant with demountable magnets, *Fusion Eng. Des.* **100** 378 (2015). doi:10.1016/j.fusengdes.2015.07.008

3 T Eich *et al*, Scaling of the tokamak near the scrape-off layer H-mode power width and implications for ITER, *Nucl. Fusion* **53** 093031 (2013). doi:10.1088/0029-5515/53/9/093031

4 R J Goldston, Heuristic drift-based model of the power scrape-off width in low-gas-puff H-mode tokamaks, *Nucl. Fusion* **52** 013009 (2012). doi:10.1088/0029-5515/52/1/013009

5 A Q Kuang *et al*, Divertor heat flux challenge and mitigation in SPARC, *J. Plasma Phys.* **86** 865860505 (2020). doi:10.1017/S0022377820001117

6 R A Pitts *et al*, Physics basis for the first ITER tungsten divertor, *Nucl. Mater. Energy* **20** 100696 (2019). doi:10.1016/j.nme.2019.100696

7 A Loarte *et al*, Chapter 4: Power and particle control, *Nucl. Fusion* **47** S203 (2007). [Progress in the ITER Physics Basis]

8 P C Stangeby, *The Plasma Boundary of Magnetic Fusion Devices* (Bristol: IOP Publishing, 2000).

9 C S Pitcher and P C Stangeby, Experimental divertor physics, *Plasma Phys. Control. Fusion* **39** 779 (1997).

10 S I Krasheninnikov, A S Kukushkin and A A Pshenov, Divertor plasma detachment, *Phys. Plasmas* **23** 055602 (2016). doi:10.1063/1.4948273

11 P M Valanju, M Kotschenreuther, S M Mahajan and J Canik, Super-X divertors and high power density fusion devices, *Phys. Plasmas* **16** 056110 (2009). doi:10.1063/1.3110984

12 M Kotschenreuther, P M Valanju, S M Mahajan and J C Wiley, On heat loading, novel divertors, and fusion reactors, *Phys. Plasmas* **14** 072502 (2007). doi:10.1063/1.2739422

13 D D Ryutov, Geometrical properties of a “snowflake” divertor, *Phys. Plasmas* **14** 064502 (2007). doi:10.1063/1.2738399

14 D D Ryutov and V A Soukhanovskii, The snowflake divertor, *Phys. Plasmas* **22** 110901 (2015). doi:10.1063/1.4935115

15 A Kallenbach *et al*, Impurity seeding for tokamak power exhaust: from present devices via ITER to DEMO, *Plasma Phys. Control. Fusion* **55** 124041 (2013). doi:10.1088/0741-3335/55/12/124041

16 B Lipschultz, F I Parra and I H Hutchinson, Sensitivity of detachment extent to magnetic configuration and external parameters, *Nucl. Fusion* **56** 056007 (2016). doi:10.1088/0029-5515/56/5/056007

17 B D Dudson *et al*, The role of particle, energy and momentum losses in 1D simulations of divertor detachment, *Plasma Phys. Control. Fusion* **61** 065008 (2019). doi:10.1088/1361-6587/ab1321

18 R J Goldston, R Myers and J Schwartz, The lithium vapor box divertor, *Phys. Scr.* **T167** 014017 (2016). doi:10.1088/0031-8949/T167/1/014017

19 A Marinoni, O Sauter and S Coda, A brief history of negative triangularity tokamak plasmas, *Rev. Mod. Plasma Phys.* **5** 6 (2021). doi:10.1007/s41614-021-00054-0

20 M E Austin *et al*, Achievement of reactor-relevant performance in negative triangularity shape in the DIII-D tokamak, *Phys. Rev. Lett.* **122** 115001 (2019). doi:10.1103/PhysRevLett.122.115001

21 N C Amorisco *et al*, FreeGSNKE: a Python-based dynamic free-boundary toroidal plasma equilibrium solver, *Phys. Plasmas* **31** 042517 (2024). doi:10.1063/5.0188467

22 T D Rognlien, J L Milovich, M E Rensink and G D Porter, A fully implicit, time dependent 2-D fluid code for modeling tokamak edge plasmas, *J. Nucl. Mater.* **196–198** 347 (1992). doi:10.1016/S0022-3115(06)80058-9

23 D Reiter, M Baelmans and P B\"orner, The EIRENE and B2-EIRENE codes, *Fusion Sci. Technol.* **47** 172 (2005). doi:10.13182/FST47-172

COLOPHON

How this document was made

The Kronos Fleet — Combined Editorial, 2026 is set in **Fraunces** (display), **Gelasio** (text), and **IBM Plex Mono** (data & equations), carried forward from the Kronos editorial design system.

The figures are rendered at 300 dpi from the deposited generator scripts; the document is composed as a single self-contained file with embedded fonts and imagery, paginated to US Letter, and rendered to PDF through a headless Chromium engine in matched light and dark editions.

Every headline quantity carries an evidence class; withdrawn and restated values are marked as such. Nothing herein is frozen beyond the founder-approved Tier-A set.

Explore it live — turn the interactive 3-D model, run the deposited solvers in the physics validator, and watch the companion film series.

LEGAL NOTICE

Notice, status, and distribution

Conceptual design & simulation study. This document reports a conceptual design and simulation study. It is not a construction commitment, a safety-analysis report, a regulatory filing, or an offer of securities. Forward-looking statements — schedules, costs, market sizes, and performance — are estimates subject to the limitations set out in the Simulations part and may change.

Numbers and their classes. Quantities are reported with evidence classes and case labels; modelled, assumed, and requirement-class values are identified as such and are not to be quoted without their labels.

Public edition. This edition carries the physics and design only; all financial, funding, and defense-commercial content has been removed for public distribution. The scientific text corresponds to the arXiv and journal submissions.

THE 2026 KRONOS SERIES

One programme, many papers

This editorial is one paper in the Kronos 2026 series — a real fusion company's complete, reproducible physics record for a spherical-tokamak breeder and its low-neutron D–^{3}He tandem-mirror burners. Every headline number is a frozen anchor in the Physics De-Risking Register.

Explore the whole programme: the De-Risking Register, the interactive 3-D model, and the physics validator.

KRONOS FUSION ENERGY

A Divertor-Exhaust Concept Down-Select for a Compact Spherical-Tokamak Breeder: Super-X, Snowflake, X-Point-Target, and Liquid-Metal Geometries Ranked by Peak Heat Flux and Detachment Window

A real fusion company building real machines. Explore the science, live.

Zenodo · doi:10.5281/zenodo.22645933

Read on kronosfusionenergy.com

The Physics De-Risking Register